EXCLUSIVE AND INCLUSIVE DIFFRACTION AT HERA

H. KOWALSKI
Deutsches Elektronen-Synchrotron, DESY
Notkestr. 85,
22607 Hamburg, Germany
E-mail: Henri.Kowalski@desy.de

This talk describes the measurement of F_2 and inclusive and exclusive diffractive cross sections in the low-x region by HERA experiments. The abundance of diffractive reactions observed at HERA indicates the presence of perturbative multi-ladder exchanges. The exclusive diffractive vector-meson and diffractive dijet production are discussed in terms of dipole models which connect the measurement of F_2 with diffractive processes and in which multiple exchanges and saturation processes are natural. The diffractive dijets are also discussed within the diffractive parton density approach. Good description of diffractive dijets in the dipole picture and in the diffractive parton density approach indicates that these two seemingly different views on diffraction are not really distinct.

1. F_2 and Diffraction at HERA

The HERA machine is a large electron-proton collider, in which electrons with energy of 27.5 GeV scatter on protons of 920 GeV. The collision products are recorded by the two large, multipurpose experiments ZEUS and H1. The detectors consist of inner tracking detectors surrounded by large calorimeters measuring the spatial energy distribution, event by event. The calorimeters are in addition surrounded by muon detector systems. Fig. 1 shows, as an example, a picture of a high Q^2 DIS event measured by the H1 and ZEUS detectors. From the amount and positions of energy deposited by the scattered electron and the hadronic debris, the total $\gamma^* p$ CMS energy, W, and the virtuality of the exchanged photon, Q^2, are determined. Counting the events at given Q^2 and W^2 allows the determination of the total cross section for the collisions of the virtual photon with the proton, $\sigma_{\gamma^* p}(W^2, Q^2)$, and in turn the structure function,

$$F_2(x, Q^2) = \frac{Q^2}{4\pi^2 \alpha_{em}} \sigma_{\gamma^* p}(W^2, Q^2)$$

with $x \approx Q^2/W^2$ when $Q^2 \ll W^2$.

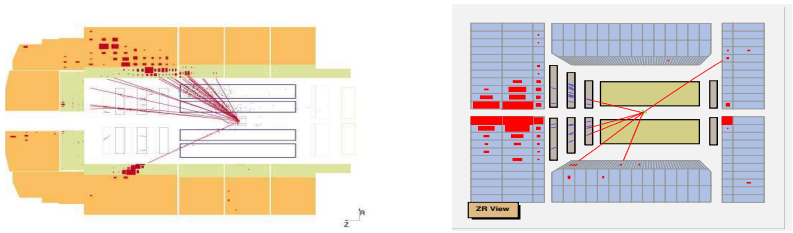

Figure 1. *Two examples of DIS events seen in the H1 (left) and ZEUS (right) detector.*

Deep inelastic scattering and the structure function F_2 have a simple and intuitive interpretation when viewed in the fast moving proton frame. The incoming electron scatters on the proton by emitting an intermediate photon with a virtuality Q^2. The incoming proton consists of a fluctuating cloud of quarks, antiquarks and gluons. Since the lifetime of the virtual photon is much shorter than the lifetime of the $q\bar{q}$-pair, the photon scans the "frozen" parton cloud and picks up quarks with longitudinal momentum x, see Fig. 2. F_2 measures then the density of partons with a size which is larger than the photon size, $1/Q$, at a given x. Fig. 3 shows the structure function F_2 as measured by H1, ZEUS and fixed target experiments for selected Q^2 values [1].

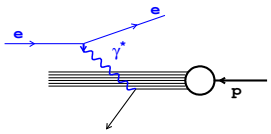

Figure 2. *Schematic view of deep inelastic scattering (DIS).*

In the low-x regime, F_2 measured at HERA exhibits a striking behavior. At low Q^2 values, $Q^2 < 1$ GeV^2, where the photon is large, F_2 rises only moderately with diminishing x, whereas as Q^2 increases, i.e. the photon becomes smaller, the rise of F_2 accelerates quickly. The rise of F_2 at low Q^2 values, i.e. when the photon is of similar size as a hadron, corresponds to the rise of the hadronic cross sections with energy. The fast rise at large Q^2 indicates the strong growth of the cloud of partons in the proton. The onset of the fast growth at Q^2 values larger than 1 GeV^2 indicates that these partons are of perturbative origin.

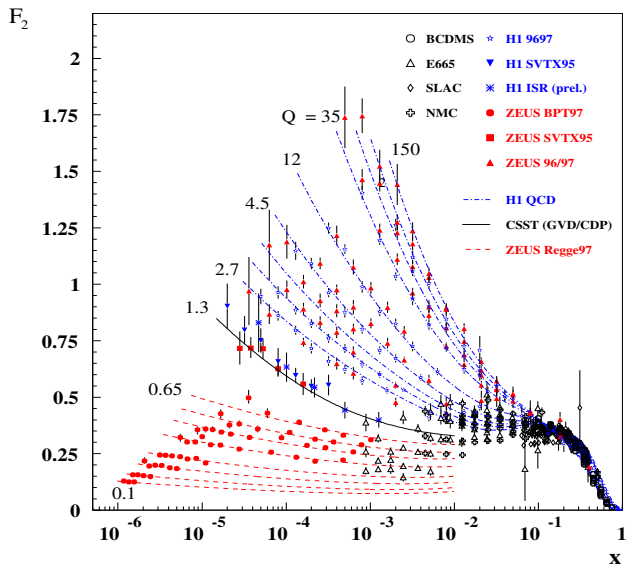

Figure 3. *The structure function F_2 as a function of x as measured by H1, ZEUS and fixed target experiments for selected Q^2 between 0.1 and 150 GeV^2.*

For sufficiently large Q^2 perturbative QCD provides a set of leading-twist linear evolution equations (DGLAP) which describe the variation of the cross section as a function of Q^2; see Fig. 4. Moreover, a closer look at the x-dependence of the parton splitting functions has led to the prediction that the gluon density, at small x, should rise with $1/x$. This rise should translate into a growth with energy of the total $\gamma^* p$ cross section or, equivalently, of F_2 with diminishing x. The data show that the growth of F_2 starts in the low-x regime which indicates that this is mainly due to the abundant gluon production. This is confirmed by all detailed theoretical

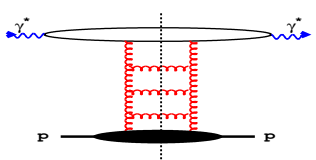

Figure 4. *Illustration of the pQCD description of the total cross section $\sigma_{tot}^{\gamma^* p}$. The gluon ladder represents the linear QCD evolution equations.*

investigations of HERA data. As an example Fig. 5 shows the results of the ZEUS and MRST analyses of parton densities. Both analyses show that in the low-x region the gluon density dwarfs all quark densities with exception of the sea quarks. The sea quarks, in perturbative QCD, are generated from the gluon density.

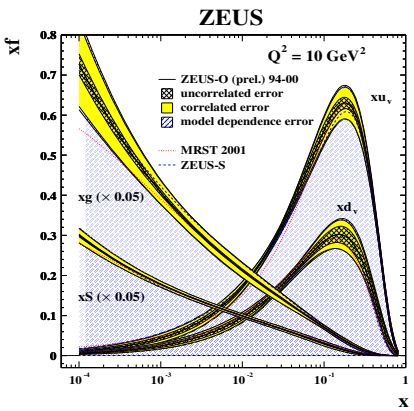

Figure 5. *Quark and gluon densities at $Q^2 = 10$ GeV^2 as determined from HERA data. Note that the gluon and sea-quark densities are displayed diminished by a factor 0.05.*

One of the most important observations of the HERA experiments is that, in addition to the usual DIS events, in which the struck proton is transformed into a swarm of particles, there are also events in which the proton remains intact after collision. Whereas the usual DIS events are characterized by large energy depositions in the forward (proton) direction, see Fig. 1, the events with intact protons show no activity in this region; see Fig. 6. By analogy to the absorption of light waves on a black disk,

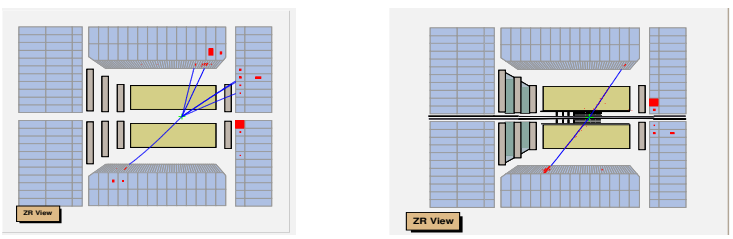

Figure 6. *Two examples of diffractive events seen in the ZEUS detector.*

the events of this type are called diffractive events and the process in which they are produced is called diffractive scattering. The intact forward proton corresponds in optics to the forward white spot observed in the center of the disc shadow.

The measurement of diffractive reactions requires the determination of two additional variables: the diffractive mass, M_X, and the square of the four-momentum transferred by the outgoing proton, t. The variable M_X, which is equal to the invariant mass of all particles emitted in the reaction with exception of the outgoing proton (or the proton dissociated system), is determined from energy depositions recorded by the central detectors of the H1 and ZEUS experiments. The variable t is determined by forward detectors, which measure the momentum of the outgoing diffractively scattered proton. In exclusive diffractive vector-meson production the t variable can also be determined from the precise measurement of the momenta of the vector-meson decay products measured in the tracking chamber systems of central detectors.

The analysis of the observed $\ln M_X^2$ distribution allows a separation of diffractive and non-diffractive events as indicated in Fig. 7. The plateau like structure, most notably seen at higher W values, is due to diffractive events since in diffraction $dN/d\ln M_X^2 \approx$ const. The high mass peaks in Fig. 7, which are due to non-diffractive events, have a steep exponential fall-off, $dN/d\ln M_X^2 \propto \exp(\lambda \ln M_X^2)$, towards smaller $\ln M_X^2$ values. This exponential fall-off is directly connected to the exponential suppression of large rapidity gaps in a single gluon ladder exchange diagram, Fig. 4, which represents the dominant QCD contribution.

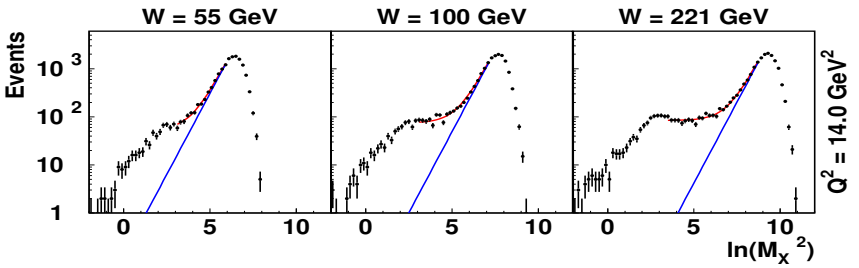

Figure 7. *Distribution of M_X in terms of $\ln M_X^2$. The straight lines give the non-diffractive contribution as obtained from the fits. Note that the $\ln M_X^2$ distribution can be viewed as a rapidity gap distribution since $\Delta Y = \ln(W^2/M_X^2)$ for $M_X^2 \gg Q^2$.*

In the ZEUS investigation [2,3] the diffractive contribution was therefore identified as the excess of events at small M_X above the exponential fall-off of the non-diffractive contribution in $\ln M_X^2$. This selection procedure is called the M_X method. In the H1 investigation [4] the selection of diffractive events was performed by the requirement of a large rapidity gap in the event. The ZEUS M_X and the H1 rapidity gap methods allow only to measure the diffractive cross section integrated over the square of the four-momentum transfer t.

The measured diffractive cross sections show a clear rise with increasing energy W in all M_X regions. It is interesting to note that the increase of the differential diffractive cross sections with W is very similar to the increase of the total inclusive DIS cross sections, i.e. $\sigma_{diff}/\sigma^{tot}_{\gamma^* p}$ is approximately independent of energy in all Q^2 and M_X regions as seen in Fig. 8. The ratio of the diffractive to the total DIS cross section integrated over the whole accessible M_X range, $M_X < 35$ GeV, was evaluated at the highest energy of $W \approx 220$ GeV. At $Q^2 = 4$ GeV^2, $\sigma_{diff}/\sigma^{tot}_{\gamma^* p}$ reaches $\sim 16\%$. It decreases slowly with increasing Q^2, reaching $\sim 10\%$ at $Q^2 = 27$ GeV^2.

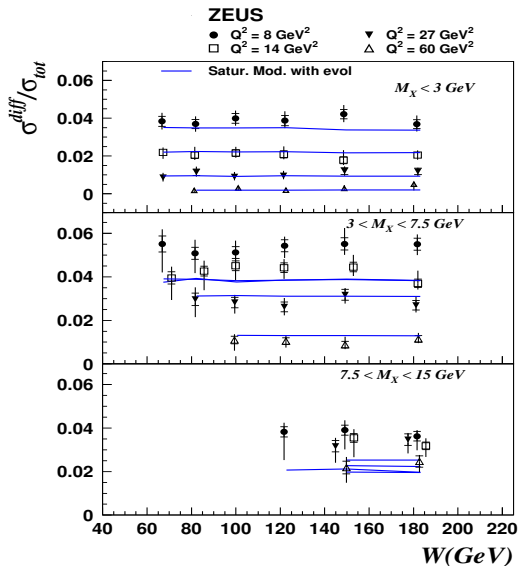

Figure 8. *The ratio of the inclusive diffractive and total DIS cross sections versus the $\gamma^* p$ energy W.*

The observation of such a large fraction of diffractive events was unex-

pected since according to the intuitive interpretation of DIS the incoming proton consists of a parton cloud and at least one of the partons is kicked out in the hard scattering process. In the language of QCD diagrams, at low-x and not so small Q^2, the total cross section or F_2 is dominated by the abundant gluon emission as described by the single ladder exchange shown in Fig. 4; the ladder structure also illustrates the linear DGLAP evolution equations that are used to describe the F_2 data. In the region of small x gluonic ladders are expected to dominate over quark ladders. The cut line in Fig. 4 marks the final states produced in a DIS event: a cut parton (gluon) hadronizes and leads to jets or particles seen in the detector. It is generally expected that partons produced from a single chain are unlikely to generate large rapidity gaps between them, since large gaps are exponentially suppressed as a function of the gap size. This is a general property of QCD evolution equations of the DGLAP, BFKL or other types.

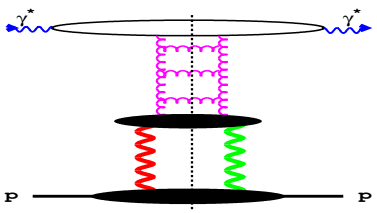

Figure 9. *Diffractive final states as part of the initial condition to the evolution equation in F_2. The thick vertical wavy lines denote the non-perturbative Pomeron exchanges which generate the rapidity gap in DIS diffractive states.*

In the single ladder contribution of Fig. 4, diffractive final states can, therefore, only reside inside the blob at the lower end, i.e. lie below the initial scale Q_0^2 which separates the parton description from the non-perturbative strong interaction, as shown in Fig. 9. The thick vertical wavy lines denote the non-perturbative Pomeron exchanges which generate the rapidity gap in DIS diffractive states [a]. The diagram of Fig. 9 exemplifies therefore the "Regge factorization" approach to diffractive parton densities as description of diffractive phenomena in DIS. In this approach the diffractive states are essentially of non-perturbative origin but they evolve accord-

[a]It is customary to call the exchange of a colourless system in scattering reactions a Pomeron. The simplest example of a (perturbative) Pomeron is given by the ladder diagram of Fig. 4.

ing to the perturbative QCD evolution equations. Note, however, that the effective Pomeron intercept, $\alpha_{I\!P}$, extracted from diffractive DIS data lies significantly above the 'soft' Pomeron intercept, indicating a substantial contribution to diffractive DIS from perturbative Pomeron exchange [3,5].

The properties of special diffractive reactions at HERA, like exclusive diffractive vector-meson and jets production, give clear indications that the diffractive processes could be hard and of perturbative origin. A significant contribution from perturbative multi-ladder exchanges should be present, in particular from the double ladder exchange of Fig. 10. This diagram provides a potential source for the harder diffractive states: the cut blob at the upper end may contain $q\bar{q}$ and $q\bar{q}g$ states which hadronize into harder jets or particles. The evidence for the presence of multi-ladder contributions is emerging mostly from the interconnections between the various DIS processes: inclusive $\gamma^* p$ reaction, inclusive diffraction, exclusive diffractive vector-meson production and diffractive jet-jet production. These interconnections are naturally expressed in the dipole saturation models, which have been shown to successfully describe HERA F_2 data in the low-x region. These models are explicitly built on the idea of summing over multiple exchanges of single ladders. In the following we will discuss the exclusive and inclusive diffractive DIS processes and their connection with the total DIS cross section in terms of dipole models.

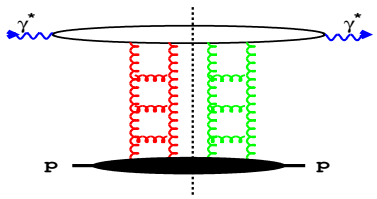

Figure 10. *The double gluon ladder contribution to the inclusive diffractive $\gamma^* p$ cross section.*

2. Dipole Models

In the dipole model, deep inelastic scattering is viewed as interaction of a colour dipole, i.e. mostly a quark-antiquark pair, with the proton. The size of the pair is denoted by r and a quark carries a fraction z of the photon momentum. In the proton rest frame, the dipole life-time is much longer

than the life-time of its interaction with the target proton. Therefore, the interaction is assumed to proceed in three stages: first the incoming virtual photon fluctuates into a quark-antiquark pair, then the $q\bar{q}$ pair elastically scatters on the proton, and finally the $q\bar{q}$ pair recombines to form a virtual photon. The amplitude for the complete process is simply the product of these three processes.

The amplitude of the incoming virtual photon to fluctuate into a quark-antiquark pair is given by the photon wave function ψ, which is determined from light cone perturbation theory to leading order in the fermionic charge (for simplicity, the indices of the quark and antiquark helicities are suppressed). Similarly the amplitude for the $q\bar{q}$ to recombine to a virtual photon is ψ^*. The cross section for elastic scattering of the $q\bar{q}$ pair with squared momentum transfer $\Delta^2 = -t$ is described by the elastic scattering amplitude, $A_{el}^{q\bar{q}}(x, r, \Delta)$, as

$$\frac{d\sigma_{q\bar{q}}}{dt} = \frac{1}{16\pi}|A_{el}^{q\bar{q}}(x, r, \Delta)|^2. \tag{1}$$

To evaluate the connections between the total cross section and various diffractive reactions it is convenient to work in coordinate space and define the S-matrix element at a particular impact parameter b

$$S(b) = 1 + \frac{1}{2}\int d^2\Delta \exp(i\vec{b}\cdot\vec{\Delta})A_{el}^{q\bar{q}}(x, r, \Delta). \tag{2}$$

This corresponds to the intuitive notion of impact parameter when the dipole size is small compared to the size of the proton. The Optical Theorem then connects the total cross section of the $q\bar{q}$ pair to the imaginary part of iA_{el}

$$\sigma_{q\bar{q}}(x, r) = \Im i A_{el}^{q\bar{q}}(x, r, 0) = \int d^2b\, 2[1 - \Re S(b)]. \tag{3}$$

The integration over the S-matrix element motivates the definition of the elastic $q\bar{q}$ differential cross section as

$$\frac{d\sigma_{q\bar{q}}}{d^2b} = 2[1 - \Re S(b)]. \tag{4}$$

The total cross section for $\gamma^* p$ scattering, or equivalently F_2, is obtained by averaging the dipole cross sections with the photon wave functions, $\psi(r, z)$:

$$\sigma^{\gamma^* p} = \int d^2r \int \frac{dz}{4\pi}\psi^*\, \sigma_{q\bar{q}}(x, r)\, \psi. \tag{5}$$

In the dipole picture the elastic vector-meson production appears in a similarly transparent way. The amplitude is given by

$$A_{\gamma^* p\to pV}(\Delta) = \int d^2r \int \frac{dz}{4\pi} \int d^2b\, \psi_V^* \psi \exp(-i\vec{b}\cdot\vec{\Delta}) 2[1 - S(b)]. \quad (6)$$

We denote the wave function for a vector meson to fluctuate into a $q\bar{q}$ pair by ψ_V. Assuming that the S-matrix element is predominantly real, we may substitute $2[1 - S(b)]$ with $d\sigma_{q\bar{q}}/d^2b$. Then, the elastic diffractive cross section is

$$\frac{d\sigma^{\gamma^* p\to Vp}}{dt} = \frac{1}{16\pi} \left| \int d^2r \int \frac{dz}{4\pi} \int d^2b\, \psi_V^* \psi \exp(-i\vec{b}\cdot\vec{\Delta}) \frac{d\sigma_{q\bar{q}}}{d^2b} \right|^2 . \quad (7)$$

The equations (5) and (7) determine the inclusive and exclusive diffractive vector-meson production using the universal elastic differential cross section $d\sigma_{q\bar{q}}/d^2b$ which contains all the interaction dynamics.

The inclusive diffractive cross section can be obtained from the eq. (7) summing over all (generalized) vector-meson states as

$$\left.\frac{d\sigma_{dif}^{\gamma^* p}}{dt}\right|_{t=0} = \frac{1}{16\pi} \int d^2r \int \frac{dz}{4\pi} \psi^*\, \sigma_{q\bar{q}}^2\, \psi. \quad (8)$$

Thus, properties of inclusive diffraction are also determined by the elastic cross section only and, contrary to vector-meson production, are not dependent on the wave function of the outgoing diffractive state.

2.1. *Dipole Cross Section and Saturation*

The dipole models became an important tool in investigations of deep inelastic scattering due to the initial observation of K. Golec-Biernat and M. Wüsthoff (GBW) [6] that a simple ansatz for the dipole cross section integrated over the impact parameter b, $\sigma_{q\bar{q}}$, is able to describe simultaneously the total inclusive and diffractive DIS cross sections:

$$\sigma_{q\bar{q}}^{GBW} = \sigma_0[1 - \exp(-r^2/4R_0^2)] \quad (9)$$

where σ_0 is a constant and R_0 denotes the x dependent saturation radius $R_0^2 = (x/x_0)^{\lambda_{GBW}} \cdot (1/GeV^2)$. The parameters $\sigma_0 = 23$ mb, λ_{GBW} and $x_0 = 3 \cdot 10^{-4}$ were determined from a fit to the data. Although the dipole model is theoretically well justified for small size dipoles only, the GBW model provides a good description of data from medium size Q^2 values ($\sim$30 GeV^2) down to low Q^2 ($\sim$0.1 GeV^2). The inverse of the saturation radius R_0 is analogous to the gluon density. The exponent λ_{GBW} determines therefore

the growth of the total and diffractive cross sections with decreasing x. For dipole sizes which are large in comparison to R_0 the dipole cross section saturates by approaching a constant value σ_0, which becomes independent of λ_{GBW}. It is a characteristic of the model that a good description of data is due to large saturation effects, i.e. the strong growth due to the factor $(1/x)^{\lambda_{GBW}}$ is, for large dipoles, significantly flattened by the exponentiation in eq. (9).

The assumption of dipole saturation provided an attractive theoretical background for investigation of the transition from the perturbative to non-perturbative regime in the HERA data. Despite the appealing simplicity and success of the GBW model it suffers from clear shortcomings. In particular it does not include scaling violation, i.e. at large Q^2 it does not match with QCD evolution (DGLAP). Therefore, Bartels, Golec-Biernat and Kowalski (BGBK) [7] proposed a modification of the original ansatz of eq.(9) by replacing $1/R_0^2$ by a gluon density with explicit DGLAP evolution:

$$\sigma_{q\bar{q}}^{BGBK} = \sigma_0[1 - \exp(-\pi^2 r^2 \alpha_s(\mu^2) x g(x, \mu^2)/3\sigma_0)] \tag{10}$$

The scale of the gluon density, μ^2, was assumed to be $\mu^2 = C/r^2 + \mu_0^2$, and the density was evolved according to DGLAP equations.

The BGBK form of the dipole cross section led to significantly better fits to the HERA F_2 data than the original GBW model, especially in the region of larger Q^2. The good agreement of the original model with the DIS diffractive HERA data was also preserved, as seen from the comparison of the predictions of the model with data for the ratio of the diffractive to the total cross section, Fig. 8.

The BGBK analysis found, surprisingly, that there exist two distinct solutions giving very good description of HERA data, depending on the quark mass in the photon wave function. The first solution is obtained assuming $m_q = 140$ MeV and leads to the initial gluon density distribution with the value of exponent $\lambda_g = 0.28$, which is very similar to the λ_{GBW}. As in the original model, the good agreement with data is due to substantial saturation effects. In the second solution, $m_q \approx 0$, and the value of the exponent is very different, $\lambda_g = -0.41$. The initial gluon density no longer rises at small x, it is valence-like, and QCD evolution plays a much more significant role than in the first solution.

The DGLAP evolution, which is generally used in the analysis of HERA data, may not be appropiate when x approaches the saturation region. Therefore, Iancu, Itakura and Munier (IIM) [8] proposed a new satura-

tion model, the Colour Glass Condensate model, in which gluon saturation effects are incorporated via an approximate solution of the Balitsky-Kovchegov equation. Later, also Forshaw and Shaw (FS) [9] proposed a Regge type model with saturation effects. The IIM and FS models provide a description of HERA F_2 and diffractive data which is better than the original GBW model and comparable in quality to the BGBK analysis. Both models find strong saturation effects in HERA data comparable to the GBW model and the first solution of the BGBK model.

All approaches to dipole saturation discussed so far ignored a possible impact parameter (IP) dependence of the dipole cross section. This dependence was introduced by Kowalski and Teaney (KT) [10], who assumed that the dipole cross section is a function of the opacity Ω:

$$\frac{d\sigma_{qq}}{d^2b} = 2\left(1 - \exp(-\frac{\Omega}{2})\right). \tag{11}$$

At small x the opacity Ω can be directly related to the gluon density, $xg(x,\mu^2)$, and the transverse profile of the proton, $T(b)$:

$$\Omega = \frac{\pi^2}{N_C}\, r^2\, \alpha_s(\mu^2)\, xg(x,\mu^2)\, T(b). \tag{12}$$

The transverse profile is assumed to be of the form:

$$T(b) = \frac{1}{2\pi B_G} \exp(-b^2/2B_G), \tag{13}$$

since the Fourier transform of $T(b)$ has the exponential form:

$$\frac{d\sigma_{VM}^{\gamma^* p}}{dt} = \exp(-B_G|t|) \tag{14}$$

The formula of eq. (11) and (12) is called the Glauber-Mueller dipole cross section. The diffractive cross section of this type was used around 50 years ago to study the diffractive dissociation of the deuterons by Glauber and reintroduced by A. Mueller [11] to describe dipole scattering in deep inelastic processes.

The parameters of the gluon density are determined from the fit to the total inclusive DIS cross section, as shown in Fig. 11 [10]. The transverse profile was determined from the exclusive diffractive J/Ψ cross sections shown in the same figure. In this approach the charm quark was explicitly taken into account with the mass $m_c = 1.25$ GeV. For a small value of Ω the dipole cross section, eq. (11), is equal to Ω and therefore proportional to the gluon density. This allows one to identify the opacity with the single Pomeron exchange amplitude of Fig. 4.

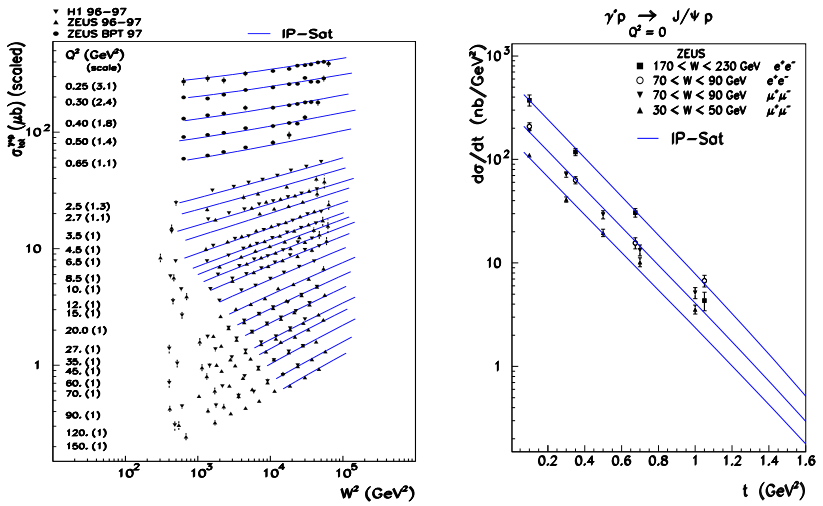

Figure 11. *LHS: The $\gamma^* p$ cross section as a function of W^2. RHS: The differential cross section for exclusive diffractive J/Ψ production as a function of the four-momentum transfer t. The solid line shows a fit by the IP saturation model (KT).*

The KT model with parameters determined in this way has predictive properties which go beyond the models discussed so far; it allows a description of the other measured reactions, e.g. the charm structure function [12] or elastic diffractive J/Ψ production [13] shown in Fig. 12. The initial gluon distribution determined in the model is valence-like, with $\lambda_g = -0.12$ and the fit pushes the quark mass to small values, $m_q \approx 50$ MeV. The resulting gluon distribution is therefore similar to the second solution of the BGBK model. The first solution of the BGBK model was disfavoured by the data. This behaviour is presumably due to the assumption of the Gaussian-like proton shape, eq. (13). In the tail of the Gaussian, the gluon density is low, but the relative contribution of the tail to the cross section is large. The saturation effects cannot therefore be as large as in the GBW-like models (i.e. BGBK-1, IIM, FS). In addition, as noted in the KT paper and also in the Thorne analysis [14], the introduction of charm in the analysis of HERA data lowers the gluon density and therefore diminishes the saturation effects. Nevertheless, the KT analysis shows that in the center of the proton ($b \approx 0$) the saturation effects are similar to the ones in the GBW-like models in which charm is properly taken into account. This can be seen from the evaluation of the saturation scale in the center of the proton in the KT

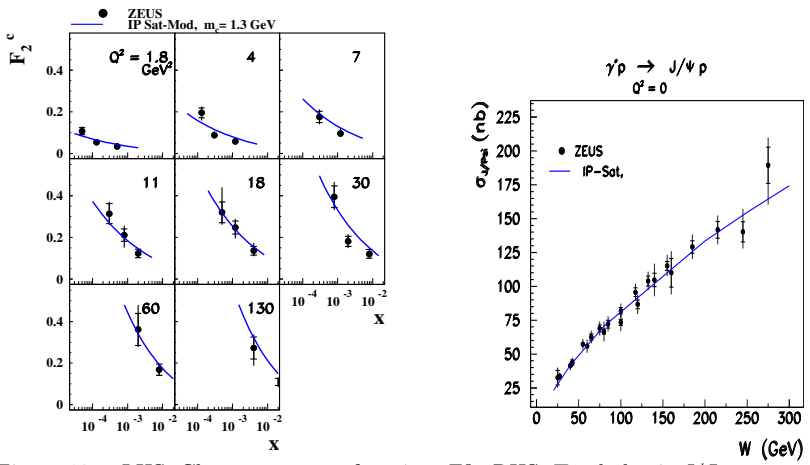

Figure 12. *LHS: Charm structure function, F_2^c. RHS: Total elastic J/Ψ cross section. The solid line shows the result of the IP saturation model (KT).*

paper and the comparison to the value of the saturation scale evaluated with charm in the original GBW paper.

3. Exclusive Diffractive Vector-Meson Production

The exclusive diffractive vector-meson production is very interesting because, in the low-x region, it is driven by the square of the gluon density. It was, therefore, investigated by many authors [15,16,17,10,18,19,20]. In addition, the information contained in the Q^2, W and t dependence of the cross sections allows to determine vector-meson wave functions together with the proton shape. The analysis can also be performed separately for the longitudinal and transverse photons.

The recent analysis of vector-meson production by Kowalski, Motyka and Watt (KMW) [21] shows that it is possible to describe the measured differential cross sections making simple assumptions about the vector-meson wave functions [15,19]. The analysis shows that using the gluon density determined from the total cross sections and the size of the interaction region determined from the t distribution of the J/Ψ meson at $Q^2 = 0$, it is possible to simultaneously describe not only the shape of various differential cross sections as a function of Q^2, W and t but also their absolute magnitude. In this analysis the assumption that vector-meson size should be much smaller than proton size was relaxed. Following the work of Bartels,

Golec-Biernat and Peters [22] the Fourier transform of eq. (7) was modified to take into account the finite size of the vector meson:

$$\exp(-i\vec{b}\cdot\vec{\Delta}) \rightarrow \exp(-i(\vec{b}+(1-z)\vec{r})\cdot\vec{\Delta}). \tag{15}$$

In this way, the information about the size of the vector meson, contained in the wave function, is contributing to the size of the interaction region B_D, together with the size of the proton. As an example of results obtained in this analysis Fig. 13 shows the comparison of KMW model predictions for the total exclusive diffractive vector-meson cross section and the size of the interaction region with data. Here, the profile function is assumed to have

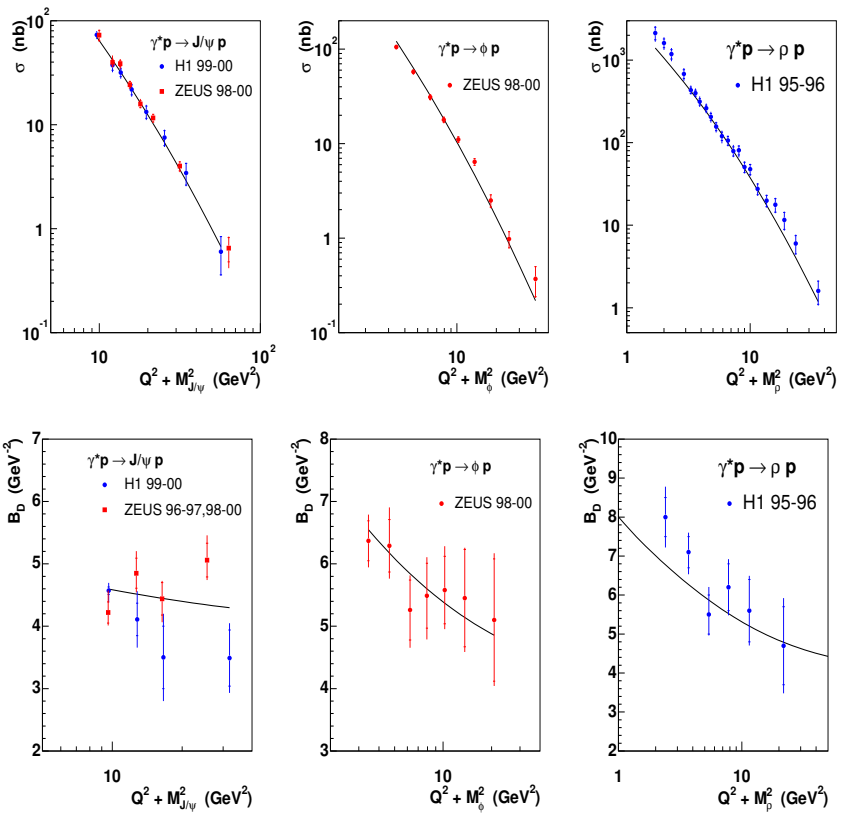

Figure 13. *(Top) The exclusive diffractive cross sections for J/Ψ, ϕ and ρ vector-meson production as a function of $Q^2 + M_V^2$. (Bottom) The interaction size B_D defined by $d\sigma/dt \propto \exp(B_D t)$, extracted from t distributions of J/Ψ, ϕ and ρ vector meson as a function of $Q^2 + M_V^2$. The solid line shows predictions of the KMW model. (Preliminary results)*

a Gaussian form (13), with the parameter $B_G = 4$ GeV^{-2}. The 'boosted Gaussian' vector-meson wave functions [19] are used. The light quark masses are $m_q = 140$ MeV, with $m_c = 1.4$ GeV.

4. Diffractive Dijets

The diffractive dijet production is analysed within QCD in two seemingly different ways: the diffractive parton density approach and the dipole picture. The diffractive structure function is proportional to the diffractive parton density which, in the simplest case, factorizes into the Pomeron flux factor and the Pomeron parton density. The Pomeron flux factor gives the probability to find a Pomeron within a proton with the momentum fraction $x_{I\!P}$. The Pomeron parton density gives the probability to find a parton within a Pomeron carrying a Pomeron momentum fraction $z_{I\!P}$[23]. This parton interacts then with the incoming photon in a boson-gluon, Fig. 14, or QCD-Compton process.

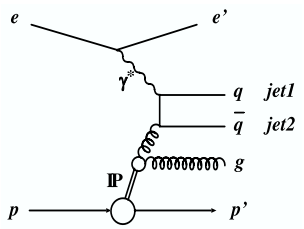

Figure 14. *Diagram describing diffractive production of a $q\bar{q}g$ state in the diffractive structure function approach.*

The diffractive parton distribution is extracted from the inclusive diffractive measurements at an initial scale, Q_0^2, and then evolved according to the DGLAP evolution to the scale Q^2 of jet production. The events are generated in the RAPGAP Monte Carlo in which the Q^2, x, $x_{I\!P}$ and $z_{I\!P}$ variables are obtained from the diffractive structure function and the jet variables, E_t, η_{jets} and β are obtained from the usual QCD matrix elements of the boson-gluon fusion and QCD-Compton processes. The results are compared to data in Fig. 16 [24].

In the dipole picture, diffractive dijet production can be directly determined from the unintegrated gluon density in the low-x region, $f(x, l^2)$, where $\vec{l}$ is the transverse momentum of the gluon coupled to the quark pair. The unintegrated gluon density is then obtained from the dipole cross sec-

tion by [7]:

$$\frac{\alpha_s f(x,l^2)}{l^4} = \frac{3}{8\pi^2}\int_0^\infty dr\, r J_0(lr)[\sigma_{q\bar{q}}(x,\infty) - \sigma_{q\bar{q}}(x,r)]. \qquad (16)$$

The jet cross sections are then computed in momentum space from diagrams shown in Fig. 15 [6]. In addition to the contributions of the $q\bar{q}$ states it is important to include the contributions of the $q\bar{q}g$ final states [25]. The

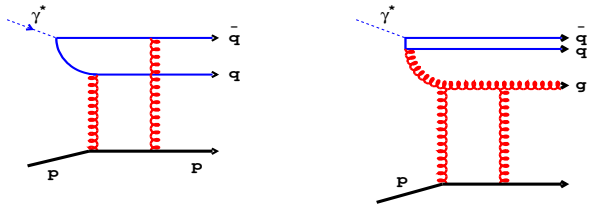

Figure 15. *Diagrams describing the diffractive production of a $q\bar{q}$ and $q\bar{q}g$ system in the dipole picture approach.*

results from the evaluation of the diagrams of Fig. 15, obtained within the SATRAP Monte Carlo, are compared to data[26,24] in Fig. 16. The figure shows that the distributions of typical jet variables are well described in both the diffractive parton densities (RAPGAP) and dipole picture (SATRAP) approaches. It is remarkable that in addition to the shapes also the absolute magnitudes of the diffractive jet cross sections are well described.

Finally, let us note for completeness that the diffractive parton density approach uses as input the inclusive diffractive data at low Q^2. It was observed that small systematic differences of input data tend to be amplified by the fitting procedure [24]. The dipole approach uses as input the dipole cross section determined from the F_2 measurements, which have smaller systematic errors than the F_2^D measurements.

5. Conclusions

One of the most important results of HERA measurements is the observation of the large amount of diffractive processes. Inclusive diffraction, diffractive jet process and exclusive diffractive vector-meson production are connected to inclusive deep inelastic scattering and, in the dipole picture,

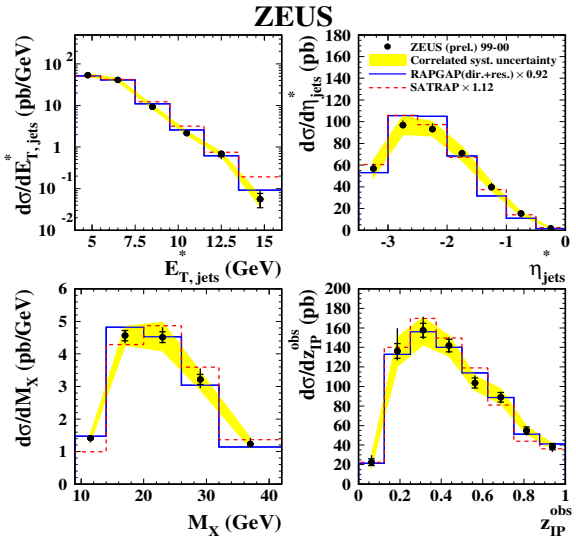

Figure 16. *The differential diffractive jet cross sections shown as a function of jet variables. The solid lines show the predictions from the LO RAPGAP MC normalised by a factor 0.92. SATRAP predictions normalised by a factor 1.12 are shown as dashed lines.*

can be successfully derived from the measured F_2. In the dipole approach, the Pomeron is essentially of the perturbative type, since the dipole models are explicitly built on the idea of summing over multiple exchanges of single ladders.

Inclusive diffraction and diffractive dijet production are also well described in the diffractive parton density approach, in which the Pomeron could be of non-perturbative origin. However, the effective Pomeron intercept extracted from diffractive DIS data lies significantly above the soft Pomeron intercept[3,5], indicating a substantial contribution to diffractive DIS from perturbative Pomeron exchange. In addition, the initial scale chosen for the analysis is relatively high, $Q_0^2 = 3$ GeV^2. At this scale F_2 exhibits a clear growth with diminishing x indicating that the exchanged Pomeron should be of perturbative type.

The good agreement between the diffractive parton density and dipole model analysis in the description of diffractive dijets indicates that both approaches, although seemingly different, are not really distinct. An attempt to combine these two approaches is recently discussed in Ref.[23].

Acknowledgments

I would like to thank Graeme Watt for discussions and help in preparing this manuscript.

References

1. G. Wolf, International Europhysics Conference on HEP, 2001
2. ZEUS Collab., J. Breitweg et al., *Eur. Phys. J.* C **6** 43 1999.
3. ZEUS Collab., S. Chekanov at al., *Nucl. Phys.* B **713** 3 2005.
4. H1 Collab., C. Adloff et al., *Z. Phys.* C **76** 613 1997.
5. H1 Collab., paper 089, EPS03, Aachen.
6. K. Golec-Biernat and M. Wüsthoff, *Phys. Rev.* D **60** 014023 1999.
7. J. Bartels, K. Golec-Biernat and H. Kowalski, *Phys. Rev.* D **66** 014001 2002.
8. E. Iancu, K. Itakura and S. Munier, *Phys. Lett.* B **590** 199 2004.
9. J. R. Forshaw and G. Shaw, JHEP **0412** 052 2004.
10. H. Kowalski and D. Teaney, *Phys. Rev.* D **68** 114005 2003.
11. A. H. Mueller, *Nucl. Phys.* B **335** 115 1990.
12. ZEUS Collab., J. Breitweg et al., *Eur. Phys. J.* C **12** 35 2000.
13. ZEUS Collab., S. Chekanov et al., *Eur. Phys. J.* C **24** 345 2002.
14. R.S. Thorne, *Phys. Rev.* D **71** 054024 2005.
15. J. Nemchik, N.N. Nikolaev, E. Predazzi and B.G. Zakharov, *Z. Phys.* C **75** 71 1997.
16. S. Munier, A. Mueller and A. Stasto, *Nucl. Phys.* B **603** 427 2001.
17. A. Caldwell and M. Soares, *Nucl. Phys.* A **696** 125 2001.
18. H.G. Dosch, T. Gousset, G. Kulzinger and H.J. Pirner, *Phys. Rev.* D **55** 2602 1997.
19. J. R. Forshaw, R. Sandapen and G. Shaw, *Phys. Rev.* D **69** 094013 2004.
20. A. Levy, *Nucl. Phys.* B **92** 146 2005.
21. H. Kowalski, L. Motyka, G. Watt, in preparation.
22. J. Bartels, K. Golec-Biernat and K. Peters, *Acta Phys. Polon.* B **34** 3051 2003.
23. G. Watt, these proceedings.
24. ZEUS Collab., XXII Int. Symp. on Lepton-Photon Interactions, Uppsala 2005, Abstract 295 and Addendum.
25. J. Bartels, J. Ellis, H. Kowalski and M. Wüsthoff, *Eur. Phys. J.* C **7** 443 1999.
26. H1 Collab., Int. Conf. on HEP ICHEP, Beijing 2004, Abstract 6-0177.